Spherical Perfectly Matched Absorber for Finite-Volume 3-D Domain Truncation

Christophe Fumeaux, *Member, IEEE*, Krishnaswamy Sankaran, *Student Member, IEEE*, and Rüdiger Vahldieck, *Fellow, IEEE*

***Abstract*—The theory of 2-D radial perfectly matched Maxwellian absorber is extended to 3-D domain truncation problems using a generalized approximate formulation of a spherical finite-volume absorber. The mathematical modeling of the spherical absorber is presented and update equations are derived. The performance of the absorber is characterized with numerical experiments. As practical application of the technique, a complex problem considering the coupling between two spiral antennas is simulated using the finite-volume time-domain method. The comparison of the results to measured data demonstrates the excellent performance of the spherical absorber.**

***Index Terms*—Finite-volume time-domain (FVTD), perfectly matched layer (PML), spherical PML.**

I. Introduction

THE finite-volume time-domain (FVTD) method, as a conformal method, offers powerful features for modeling complex geometries with curved surfaces, very fine details, and high dielectric contrast. In order to solve open-region problems using any method based on volume discretization, the computational domain must be accurately truncated with negligible reflection errors. Two major types of domain truncation techniques exist in the literature, namely, absorbing boundary condition (ABC) [1], [2] and perfectly matched layer (PML) [3]–[7] techniques. The main drawback of the ABC technique is that the truncation boundary needs to be placed sufficiently far away from the scatterer/radiator so that unphysical numerical reflections do not adversely influence the computed solution. The PML technique offers domain truncation, which has been proven to be highly accurate in conjunction with the finite-difference time-domain (FDTD) method and the finite-element method (FEM).

The FVTD method is a less established method compared to the FDTD method and FEM. Its main characteristic is the combination of conformal spatial discretization and an explicit time-domain solution of Maxwell equations. PML truncation techniques in the framework of the FVTD method have been investigated in different flavors including the Bérenger PML [8], [9] and the Maxwellian (unsplit) implementations of uniaxial models [10]. As the unstructured mesh of FVTD allows the accurate modeling of curved surfaces, there are obviously no constraints on the possible shape of the outer boundary of the computational domain. This motivates the investigation of nonrectangular PML shapes in the framework of FVTD, in particular, cylindrical and spherical PML implementations. The concept appears appealing for several reasons. First, although the PML technique offers a highly absorbing domain truncation, the corner regions are still a dominant source of reflection errors [4]. Introducing a cylindrical or spherical PML avoids corner regions and, therefore, decreases the associated reflection error [11]. Secondly, considering a structure modeled near the center of the computational domain, most of the radiated (or scattered) electromagnetic waves impinge on a spherical outer boundary at angles close to normal incidence. This further reduces the numerical error because, in general, the reflection error from the free-space to PML interface increases as the incidence approaches grazing angles. A third advantage comes from the optimal exploitation of computational space: for typical practical problems, a reduction of computational volume might be achieved when using a cylindrical or spherical outer boundary rather than a classical rectangular box. Curvilinear PML models were reported in [12]–[16] adapted for the FEM and FDTD method using cylindrical, spherical, or generalized conformal coordinate systems. Two versions of radial absorbers in Cartesian coordinates have been recently reported in the literature: One of them is a frequency-domain implementation for the FEM [17], and the other is an approximate formulation introduced for the FVTD method that projects the uniaxial absorber behavior on a cylindrical geometry [10]. The advantage of the current formulation is that it does not require a substantial change in the Maxwell equations expressed in a Cartesian coordinate system and can be easily adapted to existing codes.

In this paper, the cylindrical 2-D unsplit PML [5] formulation for the FVTD method described in [11] is extended to a 3-D radial formulation for spherical domain truncation. This paper is organized as follows. In Section II, the concept of a 2-D radial absorber is briefly summarized in the framework of FVTD. In Section III, the radial absorber theory is extended to model a 3-D spherical absorber, and an explicit formulation of the governing equations is given. Numerical examples are presented in Section IV to investigate the performance and limitations of the spherical PML. The concluding example considers the low-level coupling between two spiral antennas and demonstrates through a challenging problem the practical significance of the technique.

Manuscript received April 29, 2007; revised August 14, 2007. This work was supported by the ETH Zürich under Research Grant TH-38/04-1.

The authors are with the Laboratory for Electromagnetic Fields and Microwave Electronics, ETH Zürich, Zürich CH-8092, Switzerland (e-mail: fumeaux@ifh.ee.ethz.ch).

Color versions of one or more of the figures in this paper are available online at http://ieeexplore.ieee.org.

Digital Object Identifier 10.1109/TMTT.2007.909619

II. 2-D Radial Perfectly Matched Absorber in Conformal Mesh

The framework of the FVTD approach is briefly introduced here. The concept of the radial absorber is described using a 2-D model with invariance along the z-axis.

A. FVTD Framework

Solutions to electromagnetic field problems involve solving the partial differential equations (PDEs) represented by the two Maxwell curl equations at discrete space and time samples. In the framework of the FVTD, the computational domain is discretized using a partition of the computational volume into arbitrary polyhedral cells. Inside each ith cell of an unsplit PML, the Maxwell system can be represented in a semidiscrete conservative form as follows:

$$\partial_t \mathbf{U}_i = -\frac{1}{\alpha |V_i|} \sum_{k=1}^{f} \Psi_{U_k} - \mathbf{L}_i \tag{1}$$

where $\boldsymbol{U}_i$ denotes the unknown electromagnetic field vector and $\mathbf{L}_i$ corresponds to the perfectly matched loss vector. Each cell has a volume $|V_i|$ and is made of f faces. Each face has an area $|S_k|$ and a unit outward-normal vector $\mathbf{n}_k$. α takes the value of permeability μ and permittivity ε for the magnetic and electric field update equations, respectively. The term Ψ_{U_k} is defined as $\Psi_{U_k} = \mathbf{F}_{U_k} \cdot \mathbf{n}_k |S_k|$ with the factor $\mathbf{F}_{U_k} \cdot \mathbf{n}_k$ defining the flux function. Interested readers are referred to [18] for a detailed description of the FVTD fluxes. The information between neighboring cells sharing a common face is exchanged using this flux function. Inside the main computational domain involving free space, all the components of $\mathbf{L}_i$ are set to zero, whereas their values inside the absorber region play a crucial role in achieving reflectionless perfectly matched absorption of radiated/scattered EM waves. A second-order accurate Lax–Wendroff time-stepping scheme is used, obtaining explicit update equations for the field values [18].

The feature of the unstructured spatial discretization (e.g., triangular grid in 2-D, tetrahedral mesh in 3-D) enables conformal methods to model domain boundaries of any shape in a generalized manner while keeping the mathematical description in Cartesian coordinates. Consequently, special mesh arrangements like a curvilinear mesh or system representation in cylindrical coordinates are avoided. This is also an essential characteristics of the radial absorber described in the following.

B. Concept of 2-D Radial Absorber

In the theory of a uniaxial PML, the direction of wave attenuation is given by the direction of anisotropy. Hence, when employing a rectangular PML in order to surround a 2-D computational domain including scatterers or antennas, three different types of uniaxial media are required. The first and second type consists of an absorber with the direction of anisotropy chosen along the x- and y-axis, respectively, and the third type consists of a simple combination of first and second media, as shown on the left-hand side (LHS) of Fig. 1. The direction of anisotropy with material loss parameters (σ_x and σ_y) are defined in Fig. 1. When considering a cylindrical PML, it is natural to start the description in cylindrical coordinates (r, φ, z) with the direction of anisotropy chosen along the radial direction $\hat{r}$ (the $\hat{}$ denotes a unit vector). In fact, this radial anisotropy can be modeled locally using a rotated coordinate system given by $(\hat{x}_r, \hat{y}_r, \hat{z})$ with the direction of anisotropy given by a local x_r axis, as shown on the right-hand side (RHS) of Fig. 1. For a 2-D geometry, the local rotational transformation inside each PML cell of the finite-volume discretization has no influence on the z-component of the field vector. The field values are transformed to the global coordinate system using the reverse transformation described in [10]. This approach corresponds to an approximation that neglects the influence of radial terms in the definition of the material tensor matrix described in [15] and [17]. Although this approximation influences the absorber performances, it is of great advantage to model cylindrical problems in a simple, efficient, and sufficiently accurate manner.

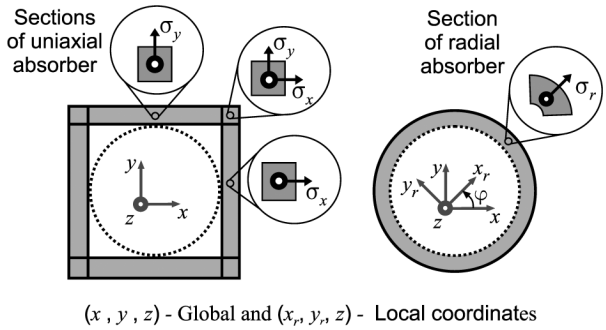

Fig. 1. (*left*) Three different kinds of uniaxial medium used in rectangular PML. (*right*) Concept of local to global transformation used in the radial absorber technique. Corresponding directions of anisotropy are given with the damping coefficient. The dotted lines enclose the common computational area. From [11].

III. 3-D Radial PML

Here, the 2-D radial (i.e., cylindrical) absorber presented above is extended to a 3-D radial (i.e., spherical) PML absorber.

A. Concept of Spherical Absorber

In the following, the radiating structure (or the scatterer) is enclosed in a spherical computational domain in the configuration depicted in Fig. 2(a). The domain truncation is set up as a spherical perfectly matched absorbing shell terminated by a perfect electrically conducting (PEC) surface. The absorbing region has a thickness d_{PML}, equivalent to typically ten average cell-edge lengths (corresponding to ten layers in an FDTD PML). In the radial absorber, each cell of the FVTD discretization is filled with a perfectly matched uniaxial medium with the direction of anisotropy in the radial direction. The model presented here locally approximates the radial absorber as a uniaxial perfectly matched absorber. To this end, a local coordinate system $(\hat{x}_r, \hat{y}_r, \hat{z}_r)$ is defined for each absorber cell, as shown on Fig. 2(b). Without loss of generality, the direction of anisotropy is chosen along the unit vector $\hat{z}_r$. The transformation R from the global coordinate system $(\hat{x}, \hat{y}, \hat{z})$ to the local coordinate system $(\hat{x}_r, \hat{y}_r, \hat{z}_r)$ is then defined by the radial direction of this unit vector $\hat{z}_r$. However, this definition is not unique, leading to an additional degree of freedom in the choice of the orientation of the other two orthogonal unit vectors $\hat{x}_r$ and $\hat{y}_r$. A simple realization of such a transformation R consists of a rotation by

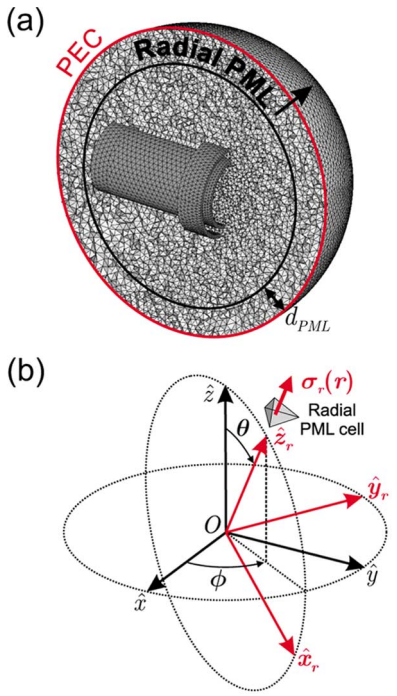

Fig. 2. (a) General configuration of the radial PML around a radiating object or scatterer. (b) Definition of the global $(\hat{x}, \hat{y}, \hat{z})$ and the local $(\hat{x}_r, \hat{y}_r, \hat{z}_r)$ coordinate systems for a radial PML cell.

an angle ϕ about the $\hat{z}$ axis followed by a rotation by an angle θ about the $\hat{y}_r$ axis [see Fig. 2(b)]. The transformation of interest for the description of the radial absorber in the global Cartesian coordinate system is defined as

$$[\hat{x}_r, \hat{y}_r, \hat{z}_r] \overset{R^{-1}}{\Rightarrow} [\hat{x}, \hat{y}, \hat{z}]. \tag{2}$$

The corresponding transformation matrix is written as

$$R^{-1} = R^T = \begin{pmatrix} \cos\phi\cos\theta & -\sin\phi & \cos\phi\sin\theta \\ \sin\phi\cos\theta & \cos\phi & \sin\phi\sin\theta \\ -\sin\theta & 0 & \cos\theta \end{pmatrix} \tag{3}$$

where the superscript T indicates matrix transposition.

B. Mathematical Description—Update Equations

The uniaxial PML medium [5] with anisotropy in the $\hat{z}_r$ direction can be described by the permittivity and permeability tensors given in the local coordinate system as

$$\left.\begin{aligned} \bar{\bar{\varepsilon}} &= \varepsilon \bar{\bar{\Lambda}}_r \\ \bar{\bar{\mu}} &= \mu \bar{\bar{\Lambda}}_r \end{aligned}\right\}, \qquad \text{with } \bar{\bar{\Lambda}}_r = \begin{pmatrix} \omega_r & 0 & 0 \\ 0 & \omega_r & 0 \\ 0 & 0 & \omega_r^{-1} \end{pmatrix}, \quad \omega_r = 1 + \frac{\sigma_r}{j\omega\varepsilon}. \tag{4}$$

A convenient way of expressing the PML governing equations is provided by the Maxwellian absorber formulation found in [4] (which can be shown to be equivalent to that of [5]). For a 3-D problem, the governing equations inside each radial PML cell are expressed locally in the $(\hat{x}_r, \hat{y}_r, \hat{z}_r)$ system as

$$\left.\begin{aligned} \varepsilon_0\partial_t E_{x_r} &= \partial_{y_r} H_{z_r} - \partial_{z_r} H_{y_r} - \sigma_r E_{x_r} \\ \varepsilon_0\partial_t E_{y_r} &= \partial_{z_r} H_{x_r} - \partial_{x_r} H_{z_r} - \sigma_r E_{y_r} \\ \varepsilon_0\partial_t E_{z_r} &= \partial_{x_r} H_{y_r} - \partial_{y_r} H_{x_r} - J_{z_r} \\ \mu_0\partial_t H_{x_r} &= -\partial_{y_r} E_{z_r} + \partial_{z_r} E_{y_r} - \sigma_r(\mu_0/\varepsilon_0) H_{x_r} \\ \mu_0\partial_t H_{y_r} &= -\partial_{z_r} E_{x_r} + \partial_{x_r} E_{z_r} - \sigma_r(\mu_0/\varepsilon_0) H_{y_r} \\ \mu_0\partial_t H_{z_r} &= -\partial_{x_r} E_{y_r} + \partial_{y_r} E_{x_r} - \mu_0 K_{z_r} \\ \varepsilon_0\partial_t J_{z_r} &= -\sigma_r\partial_{x_r} H_{y_r} + \sigma_r\partial_{y_r} H_{x_r} \\ \mu_0\partial_t K_{z_r} &= (\sigma_r/\varepsilon_0)\partial_{x_r} E_{y_r} - (\sigma_r/\varepsilon_0)\partial_{y_r} E_{x_r} \end{aligned}\right\}. \tag{5}$$

The first six equations are the standard Maxwell equations with PML loss terms. The last two PDEs can be interpreted as scalar electric J_{z_r} and magnetic K_{z_r} current quantities [4]. In order to model the radial absorber in a generalized manner, all the field quantities have to be expressed in the global coordinate system. This can be written as

$$\begin{pmatrix} E_{x_r} \\ E_{y_r} \\ E_{z_r} \end{pmatrix} = R \cdot \begin{pmatrix} E_x \\ E_y \\ E_z \end{pmatrix} \text{ and } \begin{pmatrix} H_{x_r} \\ H_{y_r} \\ H_{z_r} \end{pmatrix} = R \cdot \begin{pmatrix} H_x \\ H_y \\ H_z \end{pmatrix} \tag{6}$$

using the transformation R defined in (3). The spatial partial derivatives should also be transformed according to the chain rule, resulting in

$$\begin{aligned} \partial_{x_r} &= \cos\phi\cos\theta\partial_x + \sin\phi\cos\theta\partial_y - \sin\theta\partial_z \\ \partial_{y_r} &= -\sin\phi\partial_x + \cos\phi\partial_y \\ \partial_{z_r} &= \cos\phi\sin\theta\partial_x + \sin\phi\sin\theta\partial_y + \cos\theta\partial_z. \end{aligned} \tag{7}$$

Incorporating (6) and (7) in the first six equations of the system (5), and solving for $\partial_t E_x, \partial_t E_y, \partial_t E_z, \partial_t H_x, \partial_t H_y$ and $\partial_t H_z$ yields the PDEs for the six field components inside the radial absorber. After algebraic manipulations, these PDEs can be written in the global coordinate system as

$$\begin{aligned} \varepsilon_0\partial_t E_x = {} & \partial_y H_z - \partial_z H_y - \sigma_r E_x(1 - \cos^2\phi\sin^2\theta) \\ & + \sigma_r E_y\cos\phi\sin\phi\sin^2\theta + \sigma_r E_z\cos\phi\cos\theta\sin\theta \\ & - J_{z_r}\cos\phi\sin\theta \end{aligned} \tag{8}$$

$$\begin{aligned} \varepsilon_0\partial_t E_y = {} & \partial_z H_x - \partial_x H_z + \sigma_r E_x\cos\phi\sin\phi\sin^2\theta \\ & - \sigma_r E_y(1 - \sin^2\phi\sin^2\theta) + \sigma_r E_z\sin\phi\cos\theta\sin\theta \\ & - J_{z_r}\sin\phi\sin\theta \end{aligned} \tag{9}$$

$$\begin{aligned} \varepsilon_0\partial_t E_z = {} & \partial_x H_y - \partial_y H_x + \sigma_r E_x\cos\phi\cos\theta\sin\theta \\ & + \sigma_r E_y\sin\phi\cos\theta\sin\theta - \sigma_r E_z\sin^2\theta - J_{z_r}\cos\theta \end{aligned} \tag{10}$$

$$\begin{aligned} \mu_0\partial_t H_x = {} & \partial_z E_y - \partial_y E_z - \sigma_r(\mu_0/\varepsilon_0) H_x(1 - \cos^2\phi\sin^2\theta) \\ & + \sigma_r(\mu_0/\varepsilon_0) H_y\cos\phi\sin\phi\sin^2\theta \\ & + \sigma_r(\mu_0/\varepsilon_0) H_z\cos\phi\cos\theta\sin\theta \\ & - \mu_0 K_{z_r}\cos\phi\sin\theta \end{aligned} \tag{11}$$

$$\begin{aligned} \mu_0\partial_t H_y = {} & \partial_x E_z - \partial_z E_x + \sigma_r(\mu_0/\varepsilon_0) H_x\cos\phi\sin\phi\sin^2\theta \\ & - \sigma_r(\mu_0/\varepsilon_0) H_y(1 - \sin^2\phi\sin^2\theta) \\ & + \sigma_r(\mu_0/\varepsilon_0) H_z\sin\phi\cos\theta\sin\theta \\ & - \mu_0 K_{z_r}\sin\phi\sin\theta \end{aligned} \tag{12}$$

$$\begin{aligned}\mu_0\partial_t H_z = {} & \partial_y E_x - \partial_x E_y + \sigma_r(\mu_0/\varepsilon_0)H_x\cos\phi\cos\theta\sin\theta \\ & + \sigma_r(\mu_0/\varepsilon_0)H_y\sin\phi\cos\theta\sin\theta \\ & - \sigma_r(\mu_0/\varepsilon_0)H_z\sin^2\theta - \mu_0 K_{z_r}\cos\theta. \end{aligned} \tag{13}$$

Considering equations (8)–(13), as expected, the structure of the rotationally invariant Maxwell equations remains unchanged. The first terms on the RHS of (8)–(13) determine the fluxes in the FVTD formulation, whereas the additional terms (with no spatial derivatives) describe the anisotropic losses inside the radial absorber. The last terms of (8)–(13) contain the equivalent currents J_{z_r} and K_{z_r} (scalars), which are deliberately kept in the local coordinate system $(\hat{x}_r, \hat{y}_r, \hat{z}_r)$ in order to reduce the computational overhead. Using (6) and (7) in the last two equations of system (5), the update equations for J_{z_r} and K_{z_r} are obtained as follows:

$$\begin{aligned}\varepsilon_0\partial_t J_{z_r} = {} & \sigma_r\left(\partial_z H_y - \partial_y H_z\right)\cos\phi\sin\theta \\ & + \sigma_r\left(\partial_x H_z - \partial_z H_x\right)\sin\phi\sin\theta \\ & + \sigma_r\left(\partial_y H_x - \partial_x H_y\right)\cos\theta \end{aligned} \tag{14}$$

$$\begin{aligned}\mu_0\partial_t K_{z_r} = {} & \sigma_r(1/\varepsilon_0)(\partial_y E_z - \partial_z E_y)\cos\phi\sin\theta \\ & + \sigma_r(1/\varepsilon_0)(\partial_z E_x - \partial_x E_z)\sin\phi\sin\theta \\ & + \sigma_r(1/\varepsilon_0)(\partial_x E_y - \partial_y E_x)\cos\theta. \end{aligned} \tag{15}$$

The integration of (8)–(13) and (14) and (15) over each cell of the spatial discretization is performed according to the FVTD algorithm and yields update equations inside the radial absorber. For example, integrating (8) over the volume of the cell i yields the time update equation for the component E_x

$$\begin{aligned}\varepsilon_0\partial_t E_x = {} & \frac{-1}{|V_i|}\sum_{k=1}^{f}(\mathbf{F}_{E_{xk}}\cdot\mathbf{n}_k|S_k|) - \sigma_r E_x(1-\cos^2\phi\sin^2\theta) \\ & + \sigma_r E_y\cos\phi\sin\phi\sin^2\theta + \sigma_r E_z\cos\phi\cos\theta\sin\theta \\ & - J_{z_r}\cos\phi\sin\theta. \end{aligned} \tag{16}$$

Equations for the other field components are obtained correspondingly. Integrating (14) [and similarly (15)] over the cells of the finite-volume discretization yields

$$\begin{aligned}\varepsilon_0\partial_t J_{z_r} = {} & \frac{\sigma_r\cos\phi\sin\theta}{|V_i|}\sum_{k=1}^{f}(\mathbf{F}_{E_{xk}}\cdot\mathbf{n}_k|S_k|) \\ & + \frac{\sigma_r\sin\phi\sin\theta}{|V_i|}\sum_{k=1}^{f}\left(\mathbf{F}_{E_{yk}}\cdot\mathbf{n}_k|S_k|\right) \\ & + \frac{\sigma_r\cos\theta}{|V_i|}\sum_{k=1}^{f}(\mathbf{F}_{E_{zk}}\cdot\mathbf{n}_k|S_k|). \end{aligned} \tag{17}$$

It can be observed that the update of these scalar quantities J_{z_r} and K_{z_r} include only fluxes that are already required for the update of the E- and H-field components. Therefore, the overhead in terms of computational effort is minimal.

C. Implementation

The implementation of the spherical absorber is straightforward considering, firstly, the similarity of (8)–(13) to the standard Maxwell equations, and secondly, the simplicity of the additional PDEs (14) and (15). For each cell inside the absorber, only the following three PML-related parameters are required.

1) The radial absorber conductivity σ_r determines the losses inside the PML. To reduce the discretization error at the free-space-to-PML interface, the radial conductivity profile as a function of the radial distance r is chosen as [3]

$$\sigma_r(r) = \sigma_{r,\max}\left(\frac{r - R_{\mathrm{PML}}}{d_{\mathrm{PML}}}\right)^p \tag{18}$$

where R_{PML} is the starting radius of the PML and d_{PML} is its thickness. A quadratic conductivity profile (i.e., with order $p = 2$) is typically chosen for best performance. The value of the maximal conductivity $\sigma_{r,\max}$ is determined by the desired theoretical normal-incidence reflection coefficient Γ_0, as in [3].

2) and 3) The direction of anisotropy $\hat{z}_r$ of the radial PML for a considered cell is determined uniquely by the two angles θ and ϕ. For a spherical computational domain centered at the origin, these two angles correspond to the angular spherical coordinates at the barycenter of the cell.

For each cell in the absorber region, the three parameters σ_r, ϕ, and θ are determined uniquely based on the spatial location of the cell. Therefore, all the factors of the anisotropic loss terms in (8)–(15) can be computed once in a preprocessing step.

As a concluding remark on the formulation, it should be mentioned that (8)–(15) can be considered as a generalized formulation of the uniaxial PML with anisotropy in the direction specified by the angles (θ, ϕ). For example, the formulation of the uniaxial PML in the principal directions $\hat{x}, \hat{y}$ or $\hat{z}$ can be retrieved by considering the (θ, ϕ) angular directions $(90^\circ,\ 0^\circ)$, $(90^\circ,\ 90^\circ)$ and $(0^\circ,\ 0^\circ)$, respectively. In this perspective, it should be emphasized that the approximate radial absorber becomes an exact perfectly matched absorber only in the limit when its radius of curvature becomes infinite.

IV. Numerical Examples

Three numerical examples with increasing complexity are presented here to evaluate the accuracy of the proposed radial absorber formulation in the framework of the FVTD method.

A. Waveguide Truncation—Uniaxial PML

The first example considers the truncation of a WR90 rectangular waveguide. The waveguide is characterized by transverse dimensions $a = 22.86$ mm and $b = 10.16$ mm, and the cutoff frequency of the fundamental TE_{10} mode is 6.56 GHz. The waveguide is truncated by a 15-mm-thick PEC-backed uniaxial PML with anisotropy in the direction of the waveguide axis. The return loss of the truncated waveguide is represented in Fig. 3 for four values of the theoretical reflection coefficient ranging from $\Gamma_0 = -20$ dB to $\Gamma_0 = -80$ dB. Furthermore, the theoretical return loss $S_{11}(f)$ inside the truncated waveguide is represented via dashed lines in Fig. 3. According to the classical decomposition of the waveguide mode into plane waves, the angle of incidence γ depends on the frequency of operation f. The theoretical reflection coefficients as a function of

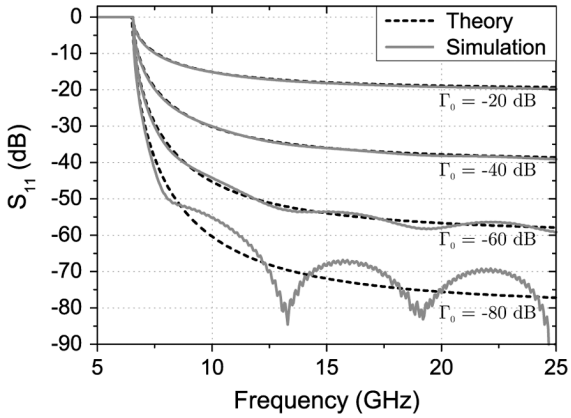

Fig. 3. Numerical return loss S_{11} of a WR90 rectangular waveguide terminated by a 15-mm-thick uniaxial PMLs for different normal-incidence theoretical reflection coefficients Γ_0. The theoretical values are computed according to (19).

the angle of incidence γ at the PML interface can be computed as [3]

$$\Gamma(\gamma) = e^{-(2/(p+1))(\sigma_{r,\max} d_{\mathrm{PML}}/\varepsilon_0 c)\cos\gamma}. \tag{19}$$

The function $\gamma(f)$ decreases from 90° (grazing incidence) at cutoff frequency to 0° (normal incidence) as the frequency asymptotically reaches infinity. As a result, the reflection coefficient $\Gamma(\gamma(f))$ corresponds to the return loss $S_{11}(f)$ inside the truncated waveguide. The results in Fig. 3 demonstrate that the 3-D FVTD absorber model is operating as intended. The low-level oscillations that are observed for the -80-dB theoretical reflection coefficient model are likely due to numerical imperfections of the source. The performance of the spherical absorber saturates below $\Gamma_0 = -80$ dB due to discretization errors. For example, decreasing Γ_0 to -100 dB does not enhance the performance for the considered spatial discretization ($\lambda/16$ at $f = 25$ GHz).

Using this waveguide model, the generalized absorber formulation (8)–(15) has been tested for radial invariance. As expected, for any orientations (θ, ϕ) of the waveguide axis in space, the return loss remains identical, provided the direction of the anisotropy is matched to the axis of the waveguide.

B. Point Source in Spherical Domain—Influence of Curvature

The second example considers an infinitesimal current source in z-direction placed in a spherical computational domain. The source is fed with a modulated Gaussian pulse with bandwidth stretching from 1 to 20 GHz. The radius of the sphere is chosen as 50 mm, which represents a fraction of the wavelength at the lower frequencies. The source is displaced from the center of the sphere in order to observe reflections from the outer boundary for a large range of incident angles. Snapshots of the z-component of the electric field at two different time stamps are shown in Fig. 4 for a source located at $x = 20$ mm, $y, z = 0$ mm (depicted as circle with a dot). On the LHS plots of Fig. 4, the domain is bounded by the Silver–Müller ABC. This first-order ABC is commonly used in FVTD because it only requires setting the incoming fluxes to zero on the outer boundary. Good absorbing performances are realized

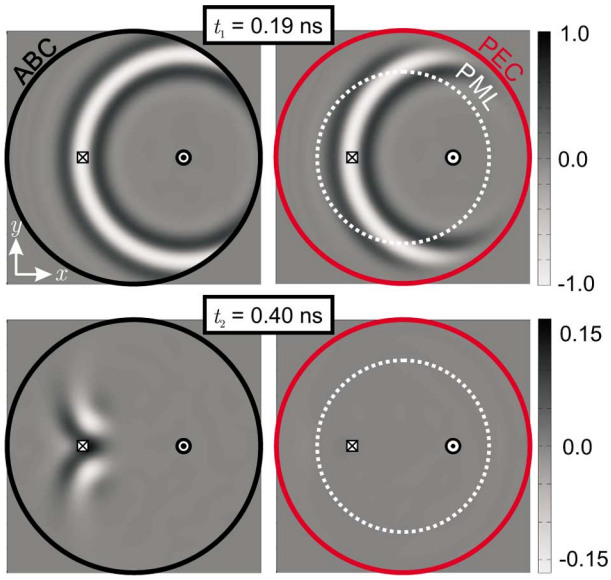

Fig. 4. Plots of the z-component of the electric field radiated from an infinitesimal current source in a spherical domain at two different time stamps. (*left*) Silver–Müller ABC truncation. (*right*) Spherical PML truncation. The source location is shown as a circle with a dot. The location of a sensor used for Fig. 6 is depicted as a crossed square. At t_1, the original pulse is visible, whereas at t_2, the incident pulse has already left the domain and only numerical reflections from the boundaries are observed.

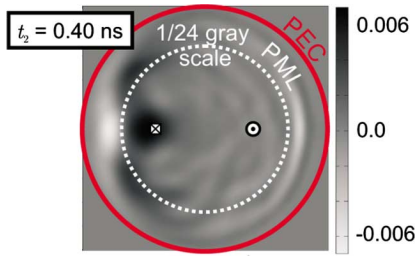

Fig. 5. Image with reduced grayscale (1/24th that of Fig. 4) showing low-level reflections from the radial absorber at time t_2.

with a spherical Silver–Müller ABC placed at a large distance from the radiator/scatterer, which results in the near-normal incidence condition. On the RHS plots of Fig. 4, the same pulse is truncated using a radial absorber with thickness $d_{\mathrm{PML}} = 16$ mm backed by a PEC. The conductivity profile is chosen as quadratic with a theoretical reflection coefficient $\Gamma_0 = -80$ dB. Absorption of the incident pulse inside the PML can be observed at the top right of Fig. 4, whereas no reflections are visible in this gray scale on the bottom right image.

The structure of the reflection from the spherical absorber becomes visible when the gray scale is substantially reduced, as shown in Fig. 5. This reveals the nature of the low-level reflected field and allows the following observations. Firstly, for a point source, the reflections from the spherical boundary are focused to a symmetric point (here, at $x = -20$ mm, $y, z = 0$ mm), marked here with a crossed square. Secondly, the slight asymmetry in the field distribution indicates that reflection errors are at a magnitude close to the level of the unstructured mesh-induced noise in the FVTD simulation for the considered discretization ($\lambda_{\min}/10$).

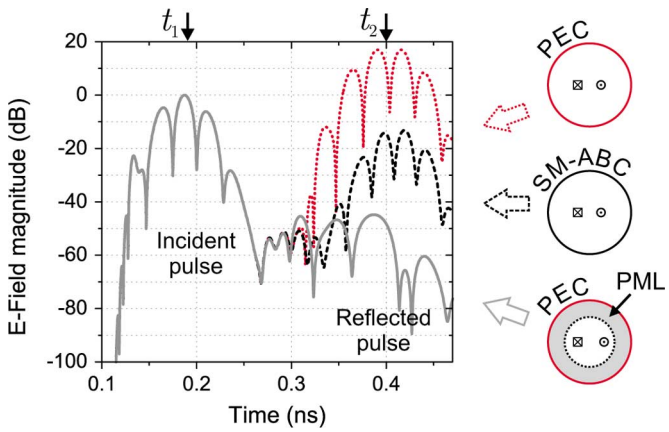

Fig. 6. E-field magnitude as a function of the time at the location of the sensor (marked as crossed square). The incident pulse is centered around t_1, and the reflected pulse around t_2 (corresponding to timestamps of Fig. 4). A reference is obtained by considering the pulse reflected by a PEC boundary without absorber (dotted line). The solid line indicates the pulse reflected by the spherical absorber. The reflection from the Silver–Müller ABC is also shown for comparison (dashed line). The radius of the full sphere (computational domain) is 50 mm, and the PML starts at $R_{\mathrm{PML}} = 34$ mm.

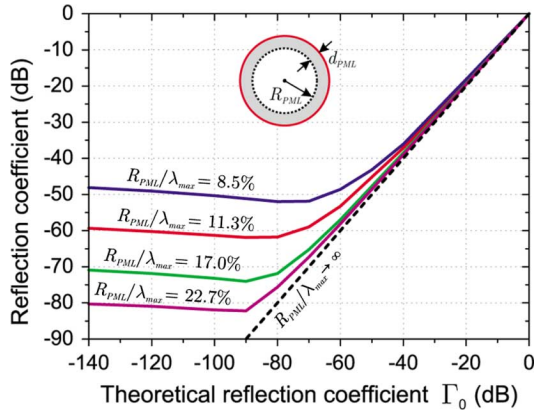

Fig. 7. Numerical reflection coefficient at the sensor location as a function of the theoretical reflection coefficient Γ_0 for different radii of curvature of the radial absorber $R_{\mathrm{PML}} = 25, 34, 51$, and 68 mm. The thickness of the absorber is kept constant $d_{\mathrm{PML}} = 16$ mm, and $\sigma_{r,\max}$ is computed to achieve the desired theoretical values Γ_0. The pulse has a bandwidth stretching from 1 to 20 GHz.

To obtain a more precise assessment of the radial absorber performance, the field components as a function of time are recorded at the location marked by a crossed square in Figs. 4 and 5. This arrangement provides a worst case assessment because the location of the "field sensor" corresponds to the point where reflections from the spherical outer boundary are focused. The field magnitude of the pulse is represented in Fig. 6 for three arrangements of the spherical outer boundary: PEC, Silver–Müller ABC, and radial absorber. The maximum of the directly incident pulse is not influenced by the outer boundary and reaches the sensor approximately at time t_1. The reflected pulse is resolved in time and reaches the sensor approximately at time t_2.

Since the reflections from different directions are focused at the sensor location, the reflected pulse in the PEC spherical cavity (dotted curve in Fig. 6) has an amplitude 17 dB higher than that of the directly incident pulse. This maximum of the reflected pulse in the PEC cavity provides a reference value, which indicates the field amplitude that need to be attenuated by the absorber. When the spherical absorber is introduced in the PEC cavity (solid curve in Fig. 6), the reflection drops significantly down to -44 dB relative to the incident pulse. This low value confirms the fact that the reflected pulse from the radial absorber is unlikely to significantly influence the results of the simulation. However, to obtain a global "reflection coefficient" integrated over all considered frequencies and angles of incidence on the outer boundaries, the pulse reflected by the absorber has to be compared to the reflected pulse in the PEC cavity without the absorber. Comparison of the reflected pulse maxima with and without absorber yields then a reflection coefficient of -61 dB from the radial absorber.

Also represented in Fig. 6 for comparison, the reflected pulse from the Silver–Müller ABC (dashed line) shows a mediocre performance of around -30 dB for the presented case.

There are three major sources of errors that explain the discrepancy between the theoretical reflection coefficient $\Gamma_0 = -80$ dB and the achieved numerical value of -61 dB, which are as follows.

1) *Discretization error:* It describes the deviation of the discrete PML from the continuous model. Convergence tests have confirmed that it is not a major contribution to the global error in the current case.
2) *Angular error:* The theoretical reflection coefficient Γ_0 is defined for normal incidence. In the example, waves impinging on the absorber at various angles degrade the performance with the angular dependence given in (19).
3) *Curvature error:* The considered approximate model of radial absorber is converging to an exact PML for infinite radius of curvature. Therefore, finite radii of curvature introduce an additional error in the absorber model.

In order to quantify these errors, the performance of the radial absorber has been assessed for different values of its inner radius R_{PML}. The rest of the arrangement remains identical, i.e., with a point source at $x = 20$ mm, and a sensor at $x = -20$ mm. The (integrated) reflection coefficients achieved numerically at the sensor location are plotted in Fig. 7 for different R_{PML} as a function of the theoretical reflection coefficient Γ_0. Results converge as the ratio $R_{\mathrm{PML}}/\lambda_{\max}$ increases, where $\lambda_{\max}$ represents the longest wavelength in the excitation pulse (1–20 GHz). This convergence is explained by the decrease of both angular and curvature errors as the radius R_{PML} increases.

To distinguish the curvature error from the angular error, further numerical experiments with a similar arrangement are conducted. Since the angular error is only dependent on the geometry, keeping the radius of the absorber R_{PML} constant and varying the frequency range $(f_{\min}, f_{\max})$ of the excitation pulse allows a characterization of the curvature error. The minimal pulse frequency is swept, while keeping the bandwidth of the pulse constant $f_{\min} : f_{\max} = 1 : 10$. This results in a variation of the radius of curvature relatively to the wavelengths involved. The numerical reflection coefficient at the sensor location is plotted in Fig. 8 as a function of $R_{\mathrm{PML}}/\lambda_{\max}$ and shows convergence of the results.

From these results, it is apparent that the low-frequency field components are decaying at a slower pace than the high-fre-

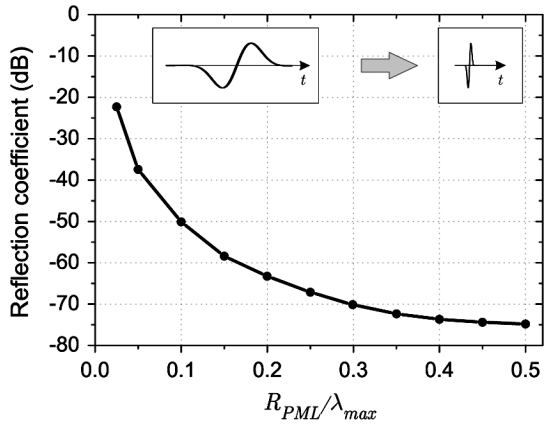

Fig. 8. Numerical reflection coefficient at the sensor location for a theoretical $\Gamma_0 = -80$ dB as a function relative radius of curvature $R_{\mathrm{PML}}/\lambda_{\max}$. The variation of $R_{\mathrm{PML}}/\lambda_{\max}$ is obtained by changing the lower frequency $f_{\min} = c/\lambda_{\max}$ of the excitation pulse for a constant $R_{\mathrm{PML}} = 51$ mm. The bandwidth of the pulse $f_{\min} : f_{\max}$ is kept to 1 : 10. The insets illustrate the pulse shapes at the first and last points in the graph.

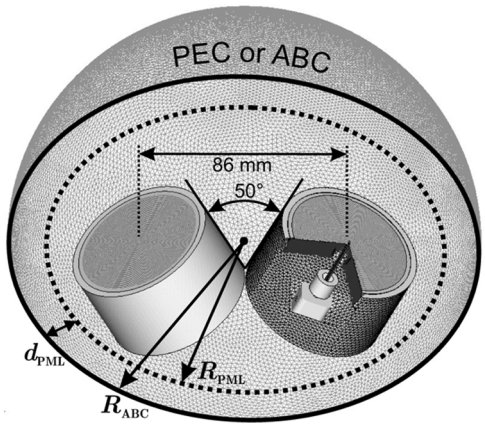

Fig. 9. Arrangement of the two cavity-backed Archimedean spiral antennas. The spiral on the right is displayed with part of its surface mesh and is cut open to reveal the balun and the cavity. The image also shows a cut through the spherical outer boundary with radius R_{ABC} and the arrangement of the radial PML.

quency components because of the smaller relative radius of curvature of the spherical absorber. This is also observed when considering the shape of the pulse reflected from the radial absorber in Fig. 6. From the presented results, it can be concluded that reasonable performances can be achieved even when the radius of curvature is a only small fraction of the minimum wavelength considered.

C. Coupling Between two Spiral Antennas

The third example shows a practical application of the radial absorber for a challenging electromagnetic problem. For most antennas applications, the performance of the Silver–Müller ABC offers a truncation accurate enough to yield results of practical engineering value. However, for scattering problems, or for the evaluation of low-level coupling between devices, the reflections from the boundary might become a dominant source of numerical error. This is illustrated with the following example that considers the coupling between two spiral antennas placed in close proximity. The two considered devices are cavity-backed Archimedean spiral antennas with an operation bandwidth of 1–18 GHz. The FVTD simulation of a single such device has been presented in [19]. The exploitation of a strongly inhomogeneous tetrahedral mesh permits the resolution of the 26 windings of the two 0.25-mm-wide arms of the spiral, the 0.25-mm-thick substrate, the absorber-loaded cavity, and the feeding balun. The typical cell size is increasing from $\sim \lambda_{\min}/100$ in the feed region to $\sim \lambda_{\min}/10$ in the free space surrounding the device and in the radial absorber. In the current configuration, the two spiral antennas are placed next to each other and tilted as shown in Fig. 9. One of the antennas is excited with a wideband pulse and the coupling parameter S_{21} to the second antenna is determined.

The first results consider the case when the computational domain is truncated with a Silver–Müller ABC (i.e., without a PML). The radius of the computational domain R_{ABC} has to be chosen large enough to achieve near normal incidence on

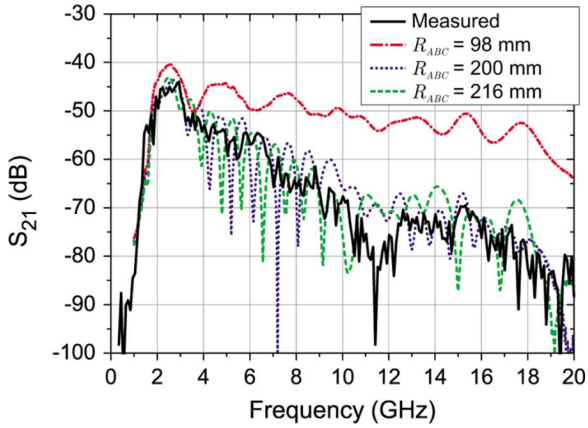

Fig. 10. Coupling parameter S_{21} of the two spiral antennas in the configuration, as shown in Fig. 9, with Silver–Müller ABC. The graph compares measured data to results obtained from FVTD simulations for domains truncated by Silver–Müller ABC with different radii R_{ABC}.

the outer Silver–Müller ABC boundary. Simulated FVTD results of the coupling coefficient S_{21} as a function of the frequency are shown in Fig. 10 together with measured data. The results for $R_{\mathrm{ABC}} = 98$ mm overestimate the parameter S_{21} because of the nonphysical dominant coupling paths including reflections from the outer boundary of the computational domain. Comparing the corresponding curves for $R_{\mathrm{ABC}} = 200$ mm and $R_{\mathrm{ABC}} = 216$ mm suggest a decrease and stabilization of the simulated coupling level as the radius R_{ABC} is increased past 200 mm. However, numerical oscillations are still observed in the coupling curve S_{21} with location of the zeros moving as R_{ABC} is increased. These oscillations decay as R_{ABC} is further increased, but at the cost of a massive increase in computational effort.

Better results are obtained with the simulation of the two spiral antennas performed in a domain truncated by a PEC-backed spherical PML. The outer radius of the computational domain can be reduced to $R_{\mathrm{ABC}} = 98$ mm. The absorber is chosen with a thickness $d_{\mathrm{PML}} = 17$ mm, a quadratic conductivity profile, and a theoretical reflection coefficient $\Gamma_0 = -80$ dB. The FVTD simulation is presented in Fig. 11 and

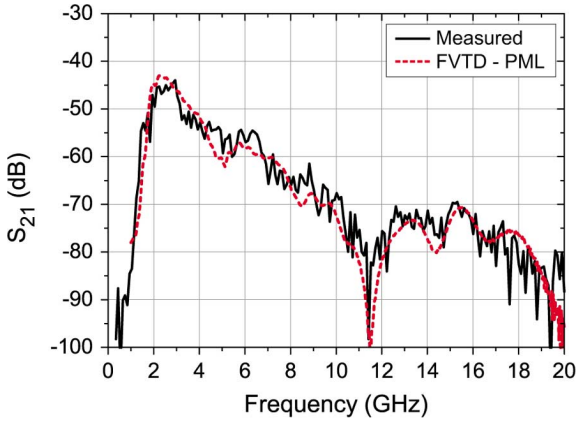

Fig. 11. Coupling parameter S_{21} of the two spiral antennas in the configuration, as shown in Fig. 9, with radial PML truncation. The graph compares measured data to results obtained from a FVTD simulation using a -80-dB PML with $R_{\mathrm{ABC}} = 98$ mm and $d_{\mathrm{PML}} = 17$ mm.

demonstrates a nearly perfect agreement to the measured data. This highlights the significant advantage of using the spherical absorber in a practical application.

V. Conclusion

This paper has presented a general approximate formulation of a spherical perfectly matched absorber suitable for conformal time-domain methods. The formulation is based on a local description of the radial absorber as a uniaxial PML, combined with a transformation into the global Cartesian coordinate system. The proposed spherical configuration has the advantage of avoiding corner regions encountered in the standard rectangular PML implementation. Furthermore, the volume of the computational domain is reduced compared to the rectangular configurations. Although the absorber accuracy is limited by its radius of curvature, several examples presented here have demonstrated excellent performances of the radial absorber as a domain truncation in the framework of the FVTD method.

The Maxwellian system describing the spherical absorber represents, in fact, a generalized formulation of the PML for any arbitrary direction of anisotropy. The absorption properties of each cell inside the absorber are uniquely described by the conductivity σ_r and the direction of anisotropy expressed by two angles (θ, ϕ). Therefore, after appropriate definition of these three parameters, the same simple and general formulation can be applied to more complex absorber shapes, e.g., ellipsoidal or convex conformal outer boundaries.

References

[1] R. L. Higdon, "Absorbing boundary conditions for difference approximations to multi-dimensional wave equation," *Math. Comput.*, vol. 47, no. 176, pp. 437–459, Oct. 1986.

[2] A. Bayliss, M. Gunzburger, and E. Turkel, "Boundary conditions for the numerical solution of elliptic equations in exterior domains," *SIAM J. Appl. Math.*, vol. 42, no. 2, pp. 430–451, 1982.

[3] J.-P. Bérenger, "A perfectly matched layer for the absorption of electromagnetic waves," *J. Comput. Phys.*, vol. 114, no. 2, pp. 185–200, 1994.

[4] R. W. Ziolkowski, "Time-derivative Lorentz material model-based absorbing boundary condition," *IEEE Trans. Antennas Propag.*, vol. 45, no. 10, pp. 1530–1535, Oct. 1997.

[5] S. Gedney, "An anisotropic perfectly matched layer-absorbing medium for the truncation of FDTD lattices," *IEEE Trans. Antennas Propag.*, vol. 44, no. 12, pp. 1630–1639, Dec. 1996.

[6] L. Zhao and A. Cangellaris, "GT-PML: Generalized theory of perfectly matched layers and its application to the reflectionless truncation of finite-difference time-domain grids," *IEEE Trans. Microw. Theory Tech.*, vol. 44, no. 12, pp. 2555–2563, Dec. 1996.

[7] T. Rylander and J.-M. Jin, "Perfectly matched layer in three dimensions for the time-domain finite element method applied to radiation problems," *IEEE Trans. Antennas Propag.*, vol. 53, no. 4, pp. 1489–1499, Apr. 2005.

[8] F. Bonnet and F. Poupaud, "Berenger absorbing boundary condition with time finite-volume scheme for triangular meshes," *Appl. Numer. Math.*, vol. 25, no. 4, pp. 333–354, Dec. 1997.

[9] K. Sankaran, C. Fumeaux, and R. Vahldieck, "Cell-centered finite-volume based perfectly matched layer for time domain maxwell system," *IEEE Trans. Microw. Theory Tech.*, vol. 54, no. 3, pp. 1269–1276, Mar. 2006.

[10] K. Sankaran, C. Fumeaux, and R. Vahldieck, "Uniaxial and radial anisotropy models for finite-volume Maxwellian absorber," *IEEE Trans. Microw. Theory Tech.*, vol. 54, no. 12, Dec. 2006.

[11] K. Sankaran, C. Fumeaux, and R. Vahldieck, "Radial absorbers for conformal time-domain methods: A solution to corner problems in mesh truncation," in *IEEE MTT-S Int. Microw. Symp. Dig.*, Honolulu, HI, Jun. 3–8, 2007, pp. 709–712.

[12] M. Kuzuoglu and R. Mittra, "Investigation of nonplanar perfectly matched absorbers for finite-element mesh truncation," *IEEE Trans. Antennas Propag.*, vol. 45, no. 3, pp. 474–486, Mar. 1997.

[13] F. L. Teixeira and W. C. Chew, "PML-FDTD in cylindrical and spherical grids," *IEEE Microw. Guided Wave Lett.*, vol. 7, no. 9, pp. 285–287, Sep. 1997.

[14] F. L. Teixeira and W. C. Chew, "Systematic derivation of anisotropic PML absorbing media in cylindrical and spherical coordinates," *IEEE Microw. Guided Wave Lett.*, vol. 7, no. 11, pp. 371–373, Nov. 1997.

[15] P. G. Petropoulos, "Reflectionless sponge layers as absorbing boundary conditions for the numerical solution of Maxwell equations in rectangular, cylindrical and spherical coordinates," *SIAM J. Appl. Math.*, vol. 60, no. 3, pp. 1037–1058, 2000.

[16] F. L. Teixeira, K. P. Hwang, W. C. Chew, and J. M. Jin, "Conformal PML-FDTD schemes for electromagnetic field simulations: A dynamic stability study," *IEEE Trans. Antennas Propag.*, vol. 49, no. 6, pp. 902–907, Jun. 2001.

[17] D. B. Davidson and M. M. Botha, "Evaluation of a spherical PML for vector FEM applications," *IEEE Trans. Antennas Propag.*, vol. 55, no. 2, pp. 494–498, Feb. 2007.

[18] P. Bonnet, X. Ferrières, B. Michielsen, P. Klotz, and J. Roumiguiéres, *Time Domain Electromagnetics*, S. M. Rao, Ed. New York: Academic, 1997, ch. 9, pp. 307–367.

[19] C. Fumeaux, D. Baumann, and R. Vahldieck, "Finite-volume time-domain analysis of a cavity-backed Archimedean spiral antenna," *IEEE Trans. Antennas Propag.*, vol. 54, no. 3, pp. 844–851, Mar. 2006.

Christophe Fumeaux (M'03) received the Diploma and Ph.D. degrees in physics from the ETH Zürich, Zürich, Switzerland, in 1992 and 1997, respectively.

From 1998 to 2000, he was a Post-Doctoral Researcher involved in infrared technology with the School of Optics, University of Central Florida, Orlando. In 2000, he joined the Swiss Federal Office of Metrology, Bern, Switzerland, as a Scientific Staff Member. Since 2001, he has been a Research Associate with the Laboratory for Electromagnetic Fields and Microwave Electronics (IFH), ETH Zürich, Zürich, Switzerland. During Fall 2005, he was a Visiting Scientist with the Laboratory of Sciences and Materials for Electronics, and of Automatic (LASMEA), Blaise Pascal University, Clermont-Ferrand, France. His current main research interest concerns computational electromagnetics in the time domain for numerical analysis of microwave circuits and antennas.

Dr. Fumeaux has been the chairman of the IEEE Swiss Joint Chapter on Microwave Theory and Techniques, Antennas and Propagation, and Electromagnetic Compatibility (EMC) since January 2006. He was the recipient of the ETH Silver Medal of Excellence for his doctoral dissertation. He was the corecipient of the 2004 Applied Computational Electromagnetics Society (ACES) Outstanding Paper Award.

Krishnaswamy Sankaran (S'98) received the B.Eng. degree (with a first-class distinction) in electrical and electronics engineering from the University of Madras, Madras, India, in 2002, the M.Sc. degree in information and communication engineering from the University of Karlsruhe TH, Karlsruhe, Germany, in 2004, and the Ph.D. degree from the ETH Zürich, Zürich, Switzerland, in 2007.

From October 2003 to May 2004, he was a Research Trainee with the European Commission, Joint Research Centre, Ispra, Italy, where he was involved in the field of radar systems engineering and remote sensing. In June 2004, he joined the ETH Zürich, where he is currently with the Laboratory for Electromagnetic Field Theory and Microwave Electronics (IFH). His main research interests are numerical methods for solving EM field problems, computational physics, and applied mathematics.

Mr. Sankaran is currently chair of the IEEE Student Branch Zürich. He was the recipient of a full postgraduate scholarship and he was one of the recipients of the 2006 Best Student Paper Award presented at the IEEE Microwave Theory and Techniques Society (IEEE MTT-S) International Microwave Symposium (IMS), San Francisco, CA.

Rüdiger Vahldieck (M'85–SM'86–F'99) received the Dipl.-Ing. and Dr.-Ing. degrees in electrical engineering from the University of Bremen, Bremen, Germany, in 1980 and 1983, respectively.

From 1984 to 1986, he was a Postdoctoral Fellow with the University of Ottawa, Ottawa, ON, Canada. In 1986, he joined the Department of Electrical and Computer Engineering, University of Victoria, Victoria, BC, Canada, where he became a Full Professor in 1991. During Fall and Spring of 1992–1993 he was a Visiting Scientist with the Ferdinand-Braun-Institute für Hochfrequenztechnik, Berlin, Germany. In 1997, he was became a Professor of electromagnetic field theory with the ETH Zürich, Zürich, Switzerland, and became Head of the Laboratory for Electromagnetic Fields and Microwave Electronics (IFH) in 2003. In 2005, he became President of the Research Foundation for Mobile Communications and was elected Head of the Department of Information Technology and Electrical Engineering (D-ITET), ETH Zürich. Since 1981, he has authored or coauthored over 300 technical papers in books, journals, and conferences. His research interests include computational electromagnetics in the general area of electromagnetic compatibility (EMC) and, in particular, for computer-aided design of microwave, millimeter-wave, and opto-electronic integrated circuits (ICs).

Prof. Vahldieck is the past president of the IEEE 2000 International Zürich Seminar on Broadband Communications (IZS'2000) and, since 2003, president and general chairman of the International Zürich Symposium on Electromagnetic Compatibility (EMC Zürich). He is a member of the Editorial Board of the IEEE TRANSACTION ON MICROWAVE THEORY AND TECHNIQUES. From 2000 to 2003, he was an associate editor for the IEEE MICROWAVE AND WIRELESS COMPONENTS LETTERS, and from July 2003 to 2005, he was the editor-in-chief. Since 1992, he has been on the Technical Program Committee (TPC) of the IEEE Microwave Theory and Techniques Society (IEEE MTT-S) International Microwave Symposium (IMS), the IEEE MTT-S Technical Committee on Microwave Field Theory, and in 1999, on the TPC of the European Microwave Conference. From 1998 to 2003, he was the chapter chairman of the IEEE Swiss Joint Chapter on IEEE MTT-S, Antennas and Propagation (AP), and Electromagnetic Compatibility (EMC) societies. He was the recipient of the 1996 Institution of Electronics and Telecommunication Engineers (IETE) J. K. Mitra Award for the best research paper. He was corecipient of the 1983 Outstanding Publication Award of the Institution of Electronic and Radio Engineers and the 2004 ACES Outstanding Paper Award.